JOURNAL OF THERMOPHYSICS AND HEAT TRANSFER
Vol. 19, No. 3, July–September 2005

Numerical Model for Bridgman–Stockbarger Crystal Growth with a Magnetic Field

Xianghong Wang* and Nancy Ma†
North Carolina State University, Raleigh, North Carolina 27695

This paper presents a model for the unsteady species transport for the growth of doped semiconductor crystals during the vertical Bridgman–Stockbarger process with a steady axial magnetic field. This dilute species transport depends on the convective and diffusive species transport of the dopant. This convective species transport is driven by buoyant convection in the melt, which produces compositional nonuniformities in both the melt and the crystal. This transient model predicts the distribution of species in the entire crystal grown in a steady axial magnetic field. The present study presents results of concentration in the crystal and in the melt at several different stages during crystal growth.

I. Introduction

DURING crystal growth without a magnetic field or with a weak magnetic field, turbulent or oscillatory melt motions can produce undesirable spatial oscillations of the concentration, or microsegregation, in the crystal.[1] Turbulent or oscillatory melt motions lead to fluctuations in the heat transfer across the growth interface from the melt to the crystal. Because the local rate of crystallization depends on the balance between the local heat fluxes in the melt and the crystal, fluctuations in the heat flux from the melt create fluctuations in the local growth rate, which create microsegregation. A moderate magnetic field can be used to create a body force that provides an electromagnetic (EM) damping of the melt motion can to eliminate oscillations in the melt motion and thus in the concentration of the crystal. Unfortunately, the elimination of mixing and a moderate or strong EM damping of the residual melt motion can lead to a large variation of the crystal's composition in the direction perpendicular to the growth direction (radial macrosegregation).

On the other hand, if the magnetic field strength is so strong that the melt motion is reduced sufficiently so that it has no effect on the composition in the crystal, then this diffusion-controlled species transport can produce a radially and axially uniform composition in the crystal grown.[2] To achieve diffusion-controlled species transport, the species transport Péclet number $Pe_m = UR/D$ must be small, where U is the characteristic velocity for the magnetically damped melt motion and is inversely proportional to the square of the magnetic flux density B, while R is the characteristic dimension of the melt and D is the diffusion coefficient for the species in the molten semiconductor. If $Pe_m \ll 1$, then the characteristic ratio of convection to diffusion of species is small, and the species transport is diffusion controlled. However, because typical values of D are extremely small, that is, 1 to 2×10^{-8} m^2/s, it would not be practical to grow a crystal in the extremely large field strength that would be required to achieve diffusion-controlled species transport. Even for crystal growth in microgravity, it is not possible to achieve diffusion-controlled species transport.[3,4] Therefore the objective is to identify a magnetic field that is strong enough to eliminate flow oscillations but which moderately damps the melt motion in order to improve both radial and axial uniformity in the crystal.

Received 8 September 2004; revision received 5 November 2004; accepted for publication 20 November 2004.

*Graduate Research Assistant, Department of Mechanical and Aerospace Engineering, Campus Box 7910.

†Assistant Professor, Department of Mechanical and Aerospace Engineering, Campus Box 7910; nancy_ma@ncsu.edu. Senior Member AIAA.

In a previous pair of studies,[5,6] we presented an asymptotic and numerical solution for the dilute species transport during the solidification of a doped crystal by the Bridgman–Stockbarger process with a strong steady axial magnetic field. This approach treated growth for strong fields for which effects of inertia and convective heat transfer are negligible[7] and involved an analytic solution to the internal energy equation, a hybrid solution for the simplified Navier–Stokes and electromagnetic equations, and a numerical solution for the full species transport equation. This treatment is only valid for strong magnetic fields, and we treated magnetic fields strengths ranging from 0.4 to 4 T. Prior to these studies, Tagawa et al.,[8] Davoust et al.,[9] and Ma and Walker[10] performed asymptotic analysis on the melt motion in Bridgman-like geometries with strong magnetic fields. The purpose of the present study is to numerically treat the full transient nonlinear equations, which are valid for any value of the magnetic field strength.

Garandet and Alboussière[11] reviewed the literature on experimental studies of Bridgman–Stockbarger growth of semiconductor crystals with magnetic fields, and Walker[12] reviewed the use of asymptotic methods in modeling of semiconductor crystal growth with strong magnetic fields.

II. Melt Motion

This paper treats the unsteady, axisymmetric species transport of silicon in a germanium melt during the vertical Bridgman–Stockbarger process with an externally applied, uniform, steady, axial magnetic field $B\hat{z}$. Here, $\hat{r}$, $\hat{\theta}$, and $\hat{z}$ are the unit vectors for the cylindrical coordinate system. During the Bridgman–Stockbarger process, the ampoule is moved from an isothermal hot zone where the germanium-silicon has been melted, through an adiabatic or thermal-gradient zone where the melt solidifies, and into a cold zone where the crystal is cooled. Our dimensionless problem is sketched in Fig. 1. The coordinates and lengths are normalized by the ampoule's inner radius R, and a is the dimensionless length of the ampoule. The melt velocity $\boldsymbol{v}$ is normalized by the characteristic velocity for the magnetically damped buoyant convection[13]

$$U = \frac{\rho g \beta (\Delta T)_c}{\sigma B^2} \tag{1}$$

where $g = 9.81$ m^2/s, ρ is the melt's density at the solidification temperature T_s, β is the thermal volumetric expansion coefficient, σ is the melt's electrical conductivity, and $(\Delta T)_c$ is the difference between the hot-zone temperature and T_s. The crystal-melt interface moves at a constant velocity $U_g = \omega U$, where ω is the dimensionless interface velocity. The planar crystal-melt interface lies at $z = -b$, where the instantaneous axial length of the melt $b(t) = a - \omega t$ decreases during growth. With time t normalized by R/U, the dimensionless time to grow the entire crystal is a/ω.

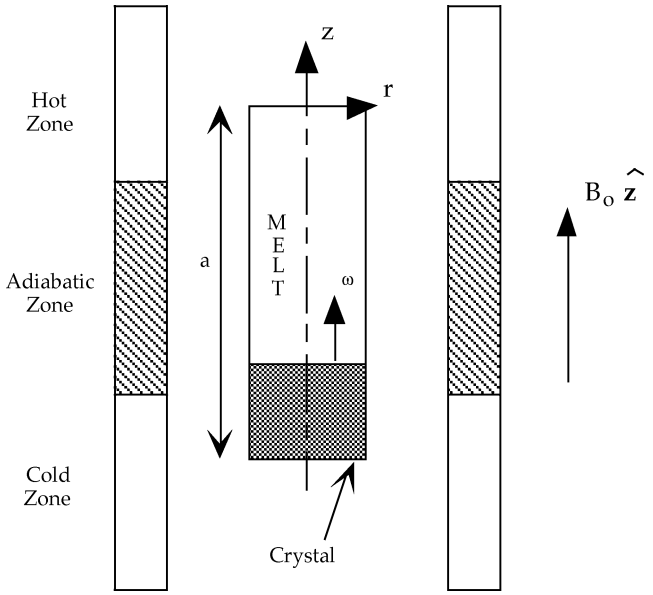

Fig. 1 Vertical Bridgman–Stockbarger ampoule with a uniform, steady, axial magnetic field $B\hat{z}$ and with coordinates normalized by the ampoule's inner radius.

The electric current in the melt produces an induced magnetic field, which is superimposed on the applied magnetic field produced by the external magnet. The characteristic ratio of the induced to the applied magnetic field strengths is the magnetic Reynolds number,

$$R_m = \mu_p \sigma U R \tag{2}$$

where μ_p is the magnetic permeability of the melt. For all crystal-growth processes, $R_m \ll 1$, and the additional magnetic fields produced by the electric currents in the melt are negligible.

Using the Boussinesq approximation, the equations governing the melt motion are

$$N^{-1}\left(\frac{\partial \boldsymbol{v}}{\partial t} + \boldsymbol{v}\cdot\nabla\boldsymbol{v}\right) = -\nabla p + T\hat{\boldsymbol{z}} + \boldsymbol{j}\times\hat{\boldsymbol{z}} + Ha^{-2}\nabla^2\boldsymbol{v} \tag{3a}$$

$$\nabla\cdot\boldsymbol{v} = 0 \tag{3b}$$

$$\nabla\cdot\boldsymbol{j} = 0 \tag{3c}$$

$$\boldsymbol{j} = -\nabla\phi + \boldsymbol{v}\times\hat{\boldsymbol{z}} \tag{3d}$$

$$Pe_t\left(\frac{\partial T}{\partial t} + \boldsymbol{v}\cdot\nabla T\right) = \nabla^2 T \tag{3e}$$

where $\boldsymbol{v}(\boldsymbol{r}, \zeta, t) = v_r\hat{\boldsymbol{r}} + v_z\hat{\boldsymbol{z}}$ is the velocity of the melt normalized by U, p is the deviation of the pressure from the hydrostatic pressure normalized by $\sigma B^2 U R$, $\boldsymbol{j}$ is the electric current density normalized by $\sigma U B$, ϕ is the electric potential function normalized by UBR, and T is the deviation of the temperature from the hot-zone temperature normalized by the characteristic temperature difference in the melt. Here R is the inner radius of the ampoule or the radius of the crystal. In the Navier–Stokes equation (3a), the interaction parameter $N = \sigma B^2 R/\rho U$ is the characteristic ratio of the electromagnetic body force to the inertial force in the melt while the Hartmann number $Ha = BR(\sigma/\mu)^{1/2}$ is the square root of the characteristic ratio of the electromagnetic body force to the viscous force in the melt. In the energy equation (3e), the characteristic ratio of the convective to conductive heat transfer is the thermal Péclet number $Pe_t = \rho c_p U R/k$, where c_p is the melt's specific heat and k is the melt's thermal conductivity.

The no-slip and no-penetration conditions are applied at the ampoule wall's and the crystal-melt interface. The thermal boundary conditions are[5]

$$T = 0 \quad \text{at} \quad z = 0 \tag{4a}$$

$$T = -1 \quad \text{at} \quad z = -b \tag{4b}$$

$$\frac{\partial T}{\partial r} = Bi(T_f - T) \quad \text{at} \quad r = 1 \tag{4c}$$

where $T_f(\zeta)$ is the dimensionless furnace temperature, while the Biot number for the heat transfer from the furnace and through the ampoule wall is $Bi = hR/k$, where h is the heat-transfer coefficient between the outside surface of the melt and the furnace. In the hot zone, $T_f = 0$ for $(-1+2d)/b < \zeta < 1$, and in the thermal-gradient zone $T_f = (\zeta+1)b/(2d) - 1$ for $-1 < \zeta(-b+2d)/b$. Here, d is the dimensionless distance between the crystal-melt interface and the vertical position in the furnace where the adiabatic and the hot zone meet. $\zeta = 1 + 2z/b$ is a rescaled axial coordinate so that $-1 \le \zeta \le +1$ for all time.

This model is idealized because we have assumed that the crystal-melt interface is planar. The heat flux is primarily axial in the thermal-gradient zone where the crystal-melt interface occurs. Because the thermal conductivity of the solid germanium is less than half that of the melt, the crystal represents a thermal barrier causing some of the heat flux to flow radially outward to the ampoule wall near the interface. This local radial heat flux causes the local isotherms and the crystal-melt interface to be concave into the crystal.[14] Future research will investigate the effect of the curved crystal-melt interface on the dopant transport.

Without a magnetic field, the local temperature gradients near the interface would drive a local buoyant convection, with very little melt motion in the isothermal region. When the electrically conducting fluid flows radially across the vertical magnetic field, it generates an induced magnetic field that drives an azimuthal electric current. This electric current flows across the magnetic field, creating an electromagnetic body force that opposes the radial velocity. There is no electromagnetic body force opposing flow along magnetic field lines. Therefore, the electromagnetic body force damps the flow that crosses magnetic field lines and elongates the flow along the magnetic field lines, so that there is buoyant convection in the entire melt.

We use a Chebyshev spectral collocation method in order to solve Eqs. (3a) and (3e) with Gauss–Lobatto collocation points in r and ζ. We use a sufficient number of collocation points in order to resolve the velocity and concentration gradients. For the time derivatives in Eqs. (3a) and (3e), we use a second-order implicit time-integration scheme to integrate from $t = 0$ to a time that is slightly less than a/ω. We chose a large enough number of time steps so that the results are not changed by increasing the number of time steps. For example, for $B = 0.4$ T, we used 71 collocation points in the radial direction, 51 collocation points in the axial direction, and 16,000 time steps. Further increasing these numbers did not change the results.

III. Dopant Transport

At the beginning of crystal growth, the melt concentration, normalized by the initial uniform concentration, is $C(r, z, t = 0) = 1$. Once crystal growth begins, the crystal absorbs much of the dopant during solidification, leaving a dopant-depleted region near the crystal-melt interface. The melt convects the melt with low Si concentration into the rest of the melt. The dimensionless equation governing this species transport is

$$\frac{\partial C}{\partial t} + \boldsymbol{v}\cdot\nabla C = Pe_m^{-1}\nabla^2 C \tag{5}$$

where C is the mole fraction of silicon in the germanium melt normalized by the melt's initial uniform concentration. Because the dopant concentrations are generally small, the dilute approximation is appropriate. We have implicitly assumed that the dopant density has no effect on the buoyant convection.

Along the crystal-melt interface,

$$\frac{2}{b}\frac{\partial C}{\partial \zeta} = Pe_g(k_s - 1)C \qquad \text{at} \qquad \zeta = -1 \tag{6}$$

where $Pe_g = U_g R/D = \omega Pe_m$ is the growth Péclet number. In Eq. (6), k_s is the segregation or partition coefficient, which is equal to 4.2 for silicon in a germanium melt. The rejection of germanium along the crystal-melt interface creates a germanium-rich region in which germanium diffuses away from the interface. The boundary conditions along the walls of the ampoule are $\hat{\boldsymbol{n}} \cdot \nabla C = 0$, where $\hat{\boldsymbol{n}}$ is the outward unit normal vector.

We use a Chebyshev spectral collocation method for the convective and diffusive terms in Eq. (5) with Gauss–Lobatto collocation points in r and ζ. We use a sufficient number of collocation points in order to resolve the velocity and concentration gradients in the melt. All values of B require a significant number of collocation points in r. Either the viscous or species-diffusion boundary layers are always thin because Ha is proportional to B while Pe_m is proportional to B^{-2}. For the time derivative in Eq. (5), we use a second-order implicit time-integration scheme to integrate from $t = 0$ to a t that is slightly less than a/ω. We chose a large enough number of time steps such that the results do not change by increasing the number of time steps. For example, for $B = 0.4$ T, we used 41 collocation points in the radial direction, 101 collocation points in the axial direction, and 16,000 time steps for the dopant transport. Further increasing these numbers did not change the results. Our results agree with our previous strong magnetic field results.[5,6] A future study will compare model predictions with experimental results.

At the beginning of crystal growth, the melt concentration normalized with the initial uniform dopant concentration is $C(r, z, t = 0) = 1$. Thus, the amount of dopant initially in the melt is obtained by integrating across the ampoule's volume giving a total dopant concentration equal to πa. We verify that the sum of the total dopant in the melt and in the crystal is equal to πa at each time step.

Assuming that there is no diffusion of dopant in the solid crystal, the dopant distribution in the crystal $C_s(r, z)$, normalized by the initial uniform dopant concentration in the melt, is given by

$$C_s(r, z) = k_s C(r, \zeta = -1, t = z/\omega) \tag{7}$$

IV. Results

For our typical germanium-silicon (GeSi) crystal growth process, $U = 192.6B^{-2}$ μm/s, $N = 33024.1B^4$, $Ha = 331.9B$, $Pe_t = 0.265B^{-2}$, $Pe_m = 72.24B^{-2}$, $Pe_g = 0.375U_g$, and $\omega = 0.00519U_g B^{-2}$ with U_g in μm/s and B in T. We present results for several cases in order to investigate the effects of the magnetic field strength B and the growth rate U_g. The dimensionless parameters for the proceeding results are presented in Table 1.

We present results for $B = 0.4$ T and $U_g = 23$ μm/s, for which $U = 0.0012$ m/s, $N = 253.7$, $Ha = 132.75$, $Pe_t = 0.4966$, $Pe_m = 451.487$, $Pe_g = 8.625$, $\omega = 0.0191$, with $a = 2$; the dimensionless time to grow a crystal is $a/\omega = 104.69$. The isotherms for the initial state for which $b = 2$ with $Bi = 10$, $d = 0.5$ are presented in Fig. 2. The thermal gradients are concentrated in a region of the melt near the crystal-melt interface because this region of the ampoule is adjacent to the furnace's thermal-gradient zone. The isotherms for the remainder of growth are very similar to those in Fig. 2 because the heat transfer is dominated by conduction for this small value of Pe_t. The streamlines for the initial state are presented in Fig. 3. In Fig. 3, the maximum value of the stream function is 0.1195. The hot fluid rises along the ampoule's periphery, flows radially inward along the top, flows axially downward along the centerline, and either solidifies or flows radially outward along the crystal-melt interface. For this case, the value of Ha is too small for an asymptotic treatment to be valid. The values of the temperature, stream function, and concentration are different from the asymptotic solution presented by Ma and Walker.[6] However, we use the asymptotic solution to provide physical insight. In an asymptotic solution for $Ha \gg 1$, the melt is divided into an inviscid core, Hartmann layers that have an $\mathcal{O}(Ha^{-1})$ thickness adjacent to the boundaries at $\zeta = \pm 1$ and carry an $\mathcal{O}(Ha^{-1})$ flow, and a parallel layer that has an $\mathcal{O}(Ha^{-1/2})$ thickness adjacent to the ampoule surface at $r = 1$ and carries an $\mathcal{O}(Ha^{1/2})$ flow. This large vertically upward flow along $r = 1$ is reflected in the crowding of the streamlines along the periphery in Fig. 3. The contours of melt concentration at various stages and the crystal concentration are presented in Fig. 4. At an early stage during growth at $t = 2.094$ when only 2% of the crystal has grown, most of the melt remains at its initial uniform concentration $C = 1$ and the minimum value of the concentration is 0.2518. At this time, the maximum value of the stream function is 0.1043. As shown in Fig. 4a, in a region near the crystal-melt interface the melt concentration is less than the initial uniform concentration because the crystal absorbs dopant during solidification. The axial magnetic field damps the flow near the melt-crystal interface, and so the dopant transport is locally controlled by diffusion

Table 1 Dimensionless parameters as a function of growth rate and magnetic field strength

U_g, μm/s	B, T	N	Ha	Pe_t	Pe_m	Pe_g	ω
23	0.4	253.7	132.75	0.4966	451.49	8.625	0.0191
23	0.1	0.9911	33.19	7.946	7224	8.625	0.001194
3	0.1	0.9911	33.19	7.946	7224	1.125	0.0001557
0.1	0.1	0.9911	33.19	7.946	7224	0.0375	0.000005191

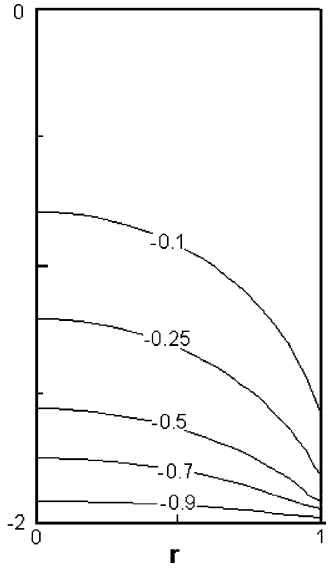

Fig. 2 Dimensionless initial isotherms for $Bi = 10$, $d = 0.5$, and $b = a = 2$.

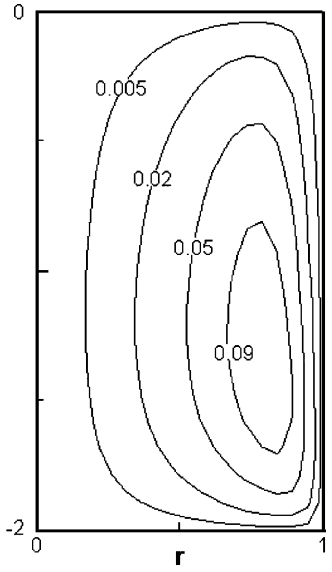

Fig. 3 Initial streamlines for the isotherms in Fig. 2 with $B = 0.4$ T and $U_g = 23$ um/s.

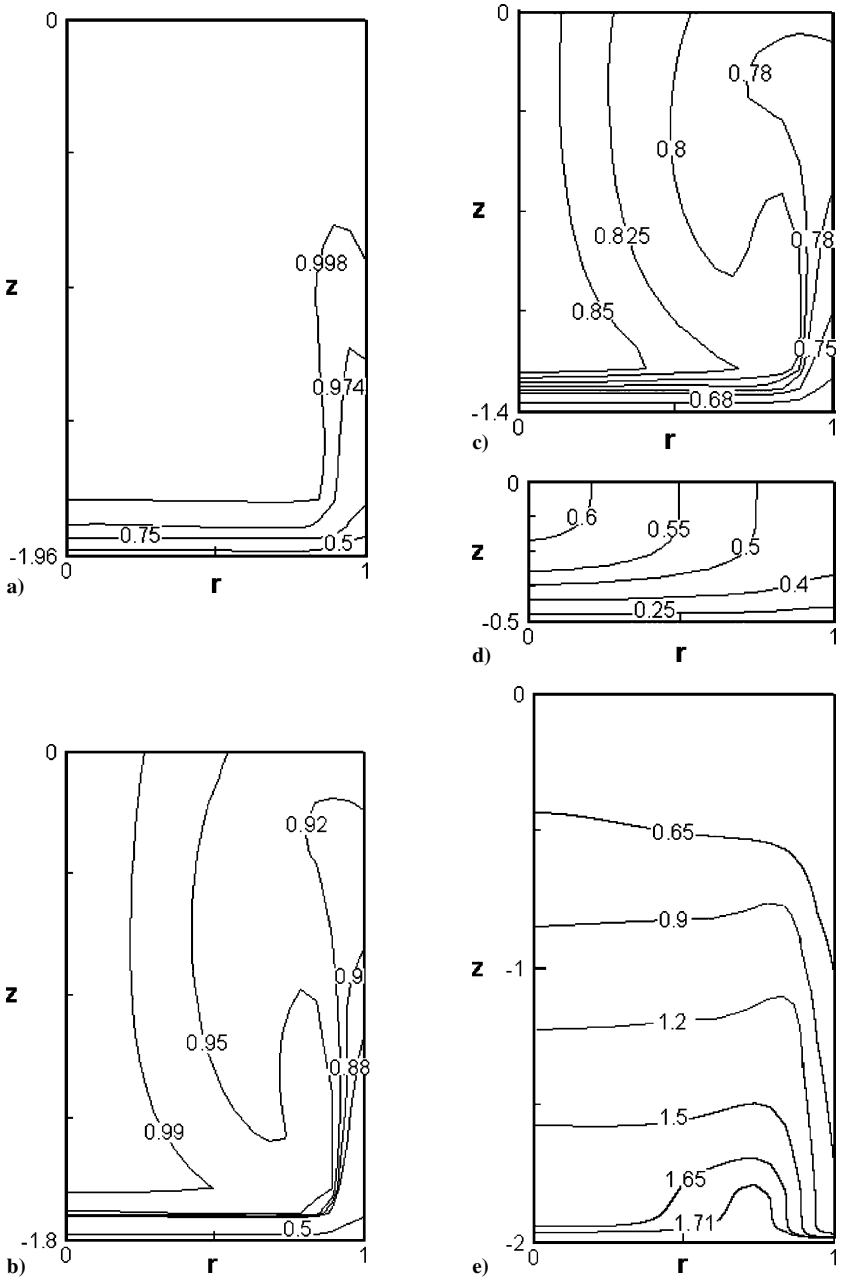

Fig. 4 Contours of concentration in the melt $C(r,z,t)$ and in the crystal $C_s(r,z)$ for $B=0.4$ T, $U_g=23$ um/s, $a=2$, and $d=0.5$: a) $C(r,z,2.094)$, b) $C(r,z,10.47)$, c) $C(r,z,31.41)$, d) $C(r,z,78.52)$, and e) $C_s(r,z)$.

in the species-diffusion boundary layer near the melt-crystal interface. The large velocities adjacent to the ampoule's vertical wall produce a strong local flow that convects the dopant-depleted fluid upward.

When $t=10.47$, 10% of the crystal has grown, and the maximum value of the stream function has decreased to 0.09750. The flowfield resembles that shown in Fig. 3, but the maximum stream function has decreased because the melt depth has decreased and the strength of the thermal buoyant convection is proportional to b^{-1}. At this time, the melt's minimum and maximum concentrations in Fig. 4b are 0.2120 and 0.9998, respectively. The average dopant concentration in the melt has decreased because of absorption of dopant along the crystal-melt interface. By this time, the dopant-depleted melt has convected throughout the entire melt so that the melt's concentration has decreased to $C<1$ everywhere. When $t=31.41$, 30% of the crystal has grown, and the minimum and maximum values of the melt's concentration have further decreased to 0.1893 and 0.8750, respectively, as shown in Fig. 4c. At this stage of growth, the maximum value of the stream function is 0.07553. For most of the remainder of crystal growth, the contours of the melt's concentration resemble those in Fig. 4c. The melt's concentration continues to decrease because of absorption of dopant along the crystal-melt interface. By the time 75% of the crystal has grown, the ratio of convective to diffusive dopant transport has decreased so that the diffusion of dopant has become much stronger as shown in Fig. 4d. This occurs because the magnitude of the buoyant convection has decreased so much that the maximum value of the stream function is only 0.00001595 and because the $\mathcal{O}(Pe_g^{-1})$ thickness of the species-diffusion boundary layer adjacent to the crystal-melt interface is approximately 0.12 so that it extends over a quarter of the remaining melt. In Fig. 4d, the minimum and maximum values of the melt's concentration have decreased to 0.1201 and 0.6135, respectively.

The constant-concentration curves in the crystal are presented in Fig. 4e. For the streamlines presented in Fig. 3, as r increases from 0 to 1, 1) the value of v_z near the crystal-melt interface is

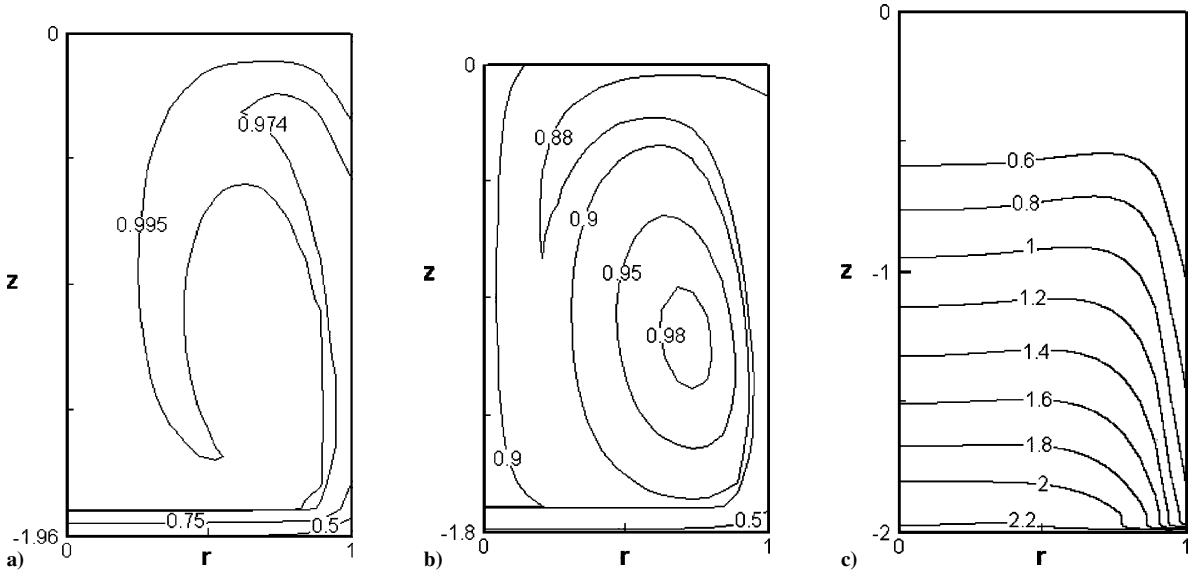

Fig. 5 Contours of concentration in the melt $C(r,z,t)$ and in the crystal $C_s(r,z)$ for $B=0.1$ T, $U_g=23$ um/s, $a=2$, and $d=0.5$: a) $C(r,z,33.501)$, b) $C(r,z,167.51)$, and c) $C_s(r,z)$.

negative and increases in magnitude until at some radial position, say, at $r=r_o$; 2) then v_z increases rapidly from this minimum to a large positive value, corresponding to the upward flow adjacent to $r=1$; and 3) finally v_z decreases to zero at $r=1$. For $0<r<r_o$, the downward buoyant convection augments the upward motion of the crystal-melt interface, so that there is strong buoyant convection of the melt with $C=1$ towards the interface. Because v_z has its largest negative value near $r=r_o$, the convection of Si towards the interface is strongest here, explaining the humps in the $C_s=1.71$ and $C_s=1.65$ contours in Fig. 4e. For $r>r_o$, v_z has a large positive value, so that the buoyant convection and crystal-melt interface motion partially cancel, producing much smaller local melt motion relative to the interface. Thus, the local melt does not receive more Si by convection, and the local value of C decreases quickly as the crystal absorbs most of the local Si. For the later-grown section of the crystal, C is much more radially uniform for $r<r_o$, with much lower values for $r>r_o$. The uniformity for $r<r_o$ is explained by the melt's concentrations in Figs. 4b and 4c. The strong downward buoyant convection near $r=r_o$, which previously convected $C=1$ towards the interface now convects Si-depleted melt, which has circulated from the crystal-melt interface to the top and back to the interface. The slower moving fluid near $r=0$ has a much higher concentration because it left the species-diffusion boundary layer at a much earlier time before the Si was so depleted. For the $C_s=0.65$ contour in Fig. 4e, C_s actually decreases as r increases from 0 to r_o because the stronger downward flow near $r=r_o$ is carrying very little Si while the slower moving melt near $r=0$ retains a higher concentration. The dopant concentration decreases as the axial position along the crystal increases because $k_s>1$.

To investigate the effects of decreasing the magnetic field strength, we present contours of the concentration in the melt in Figs. 5a and 5b, respectively, for $B=0.1$ T and $U_g=23$ μm/s for which $U=0.01926$ m/s, $N=0.9911$, $Ha=33.19$, $Pe_t=7.946$, $Pe_m=7224$, $Pe_g=8.625$, $\omega=0.001194$, and the dimensionless time to grow a crystal is $a/\omega=1675$. This much weaker magnetic field strength provides a much smaller electromagnetic damping of the melt motion. For instance, when 2% of the crystal has grown at $t=33.501$, the maximum value of the stream function is 0.03489. The buoyant convection is much stronger than the buoyant convection for $B=0.4$ T because the electromagnetic body force is not as strong for $B=0.1$ T. This drives a much larger convective dopant transport as reflected in Fig. 5a at $t=33.501$ in which the dopant-depleted melt has already convected vertically up the periphery, radially inward along the top of the ampoule and vertically downward. At this stage of growth, there is only a small pocket

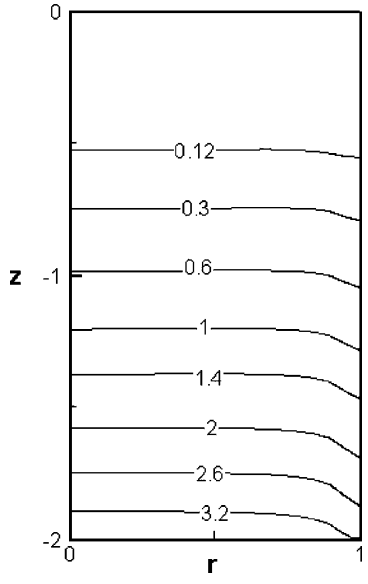

Fig. 6 Contours of concentration in the crystal $C_s(r,z)$ for $B=0.1$ T and $U_g=3$ um/s.

of melt that has concentration $C=1$, and the minimum value of the concentration is 0.2646. By the time 10% of the crystal has grown at $t=167.51$, the dopant-depleted melt has convected everywhere in the melt as shown in Fig. 5b. The minimum value of the melt's concentration is 0.2374, and the maximum value of the melt's concentration has decreased to 0.9864. The convective dopant transport is so strong that the constant-concentration curves have closed on themselves, as reflected in the $C=0.9$, 0.95, and 0.98 contours in Fig. 5b. In Figs. 5a and 5b, the melt's concentration is lowest along the crystal-melt interface at $r=1$ as a result of the absorption of dopant along the interface and the quick convection of the melt axially upward along the periphery. This is reflected in the crystal concentration, which is presented in Fig. 5c in which the concentration is lowest near the periphery of the ampoule. The strong convective dopant transport causes most of the crystal to solidify with a relatively radially uniform concentration except near $r=1$.

We investigate the effects of decreasing the growth rate for $B=0.1$ T. As we decrease the growth rate, the buoyant convection has more time to circulate so that the convective dopant transport increases and provides a more radially uniform dopant distribution. For $U_g=3$ μm/s, the crystal's concentration in Fig. 6 reflects a more

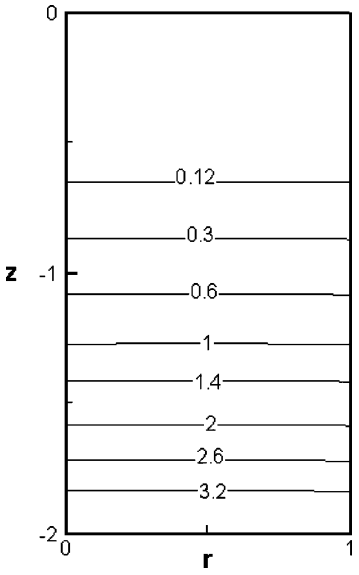

Fig. 7 Contours of concentration in the crystal $C_s(r, z)$ for $B = 0.1$ T and $U_g = 0.1$ um/s.

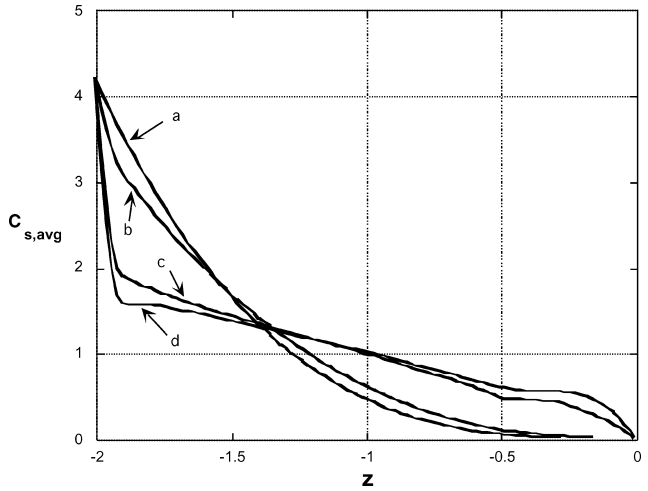

Fig. 8 Axial variation of the radially averaged crystal concentrations for four cases with $a = 2$: a) $B = 0.1$ T and $U_g = 0.1$ μm/s, b) $B = 0.1$ T and $U_g = 3$ μm/s, c) $B = 0.1$ T and $U_g = 23$ μm/s, and d) $B = 0.4$ T and $U_g = 23$ μm/s.

radially uniform dopant distribution compared with $U_g = 23$ μm/s in Fig. 5c. In Fig. 6, the dopant concentration in the crystal is slightly lower near the periphery. When we further decrease the growth rate to $U_g = 0.1$ μm/s, the growth rate is so slow that the crystal's dopant concentration is virtually radially uniform, as shown in Fig. 7.

In the classical well-mixed limit, the dopant is instantly mixed over the volume of the melt at each time. In the classical diffusion-controlled limit, the crystal concentration is nearly uniform at the melt's initial uniform composition $C = 1$ except for the first-grown part and last-grown parts of the crystal. The parameter that predicts the relative position of the actual axial variation between the well-mixed and diffusion-controlled limits is the number of complete circuits made by the buoyant convection during the length of time to grow the crystal, and the number of the complete circuits is proportional to ω^{-1}. When the growth rate decreases, the number of the complete circuits made by the buoyant convection increases. Therefore, the position of the actual axial variation is closer to the well-mixed limit. When a magnetic field is applied to the melt, the magnetic field provides an EM body force, which damps the convective transport of dopant. As the magnetic field strength is increased, the damping of the convection is increased. This means that the ratio of the diffusive dopant transport to the convective dopant transport increases, and so the position of the actual axial variation is closer to the diffusion-controlled limits. All of these are demonstrated in the Fig. 8, which shows the axial variation of the radially averaged concentration for four cases with $a = 2$ and $d = 0.5$. For the case $B = 0.1$ T and $U_g = 0.1$ μm/s, the magnetic field is weak so that the convective dopant transport is strong. The growth rate is slow, and so the strong convection makes many completed circuits during the long time to grow a crystal. This result approaches the well-mixed limit. For the cases $B = 0.1$ T and $U_g = 0.1$ μm/s as well as $B = 0.1$ T and $U_g = 3$ μm/s, the magnetic field strengths are the same, but the former case has a smaller growth rate than the later case; therefore, the convection makes more complete circuits, and the curve is closer to the well-mixed limit. For the cases $B = 0.4$ T and $U_g = 23$ μm/s as well as $B = 0.1$ T and $U_g = 23$ μm/s, the growth rates are the same, but the buoyant convection is more damped by the stronger magnetic field, and so there are fewer complete circuits, and the curve for $B = 0.4$ T and $U_g = 23$ μm/s is farther from the well-mixed limit and closer to the diffusion-controlled limit than the curve for $B = 0.1$ T and $U_g = 23$ μm/s.

V. Conclusions

We have developed a numerical model that can accurately predict the unsteady transport in the melt and the dopant distribution in the crystal. During the vertical Bridgman crystal growth with an axial magnetic field, the convective transport of dopant is stronger than the diffusive transport of dopant for the weak or moderate magnetic fields. When the strength of the magnetic field is increased, the damping of convection is increased, and the relative importance of diffusion is increased. This causes the crystal to grow with a more axially uniform dopant distribution and a less radially uniform dopant distribution. As the growth rate is decreased, the crystal grows with a more radially uniform dopant distribution and a less axially uniform dopant distribution.

Acknowledgments

This research was supported by the U. S. Air Force Office of Scientific Research under Grant FA9550-04-1-0249. The calculations were performed on the Cray X1 and the SGI Origin 3000 Complex provided by the U.S. Department of Defense High Performance Computing Modernization Program under Grant AFSNH2487 and on the IBM pSeries 690 provided by the National Computational Science Alliance.

References

[1]Walker, J. S., Henry, D., and BenHadid, H., "Magnetic Stabilization of the Buoyant Convection in the Liquid-Encapsulated Czochralski Process," *Journal of Crystal Growth*, Vol. 243, No. 1, 2002, pp. 108–116.

[2]Wang, X., and Ma, N., "Strong Magnetic Field Asymptotic Model for Binary Alloyed Semiconductor Crystal Growth," *Journal of Thermophysics and Heat Transfer*, Vol. 18, No. 4, 2004, pp. 476–480.

[3]Ma, N., and Walker, J. S., "Magnetic Damping of Buoyant Convection During Semiconductor Crystal Growth With g-Jitters," *Journal of Thermophysics and Heat Transfer*, Vol. 11, No. 2, 1997, pp. 212–215.

[4]Ma, N., and Walker, J. S., "Magnetic Damping of Buoyant Convection During Semiconductor Crystal Growth in Microgravity. Continuous Random g-Gitters," *Physics of Fluids*, Vol. 8, No. 1/4, 1996, pp. 944–953.

[5]Ma, N., and Walker, J. S., "A Model of Dopant Transport During Bridgman Crystal Growth with Magnetically Damped Buoyant Convection," *Journal of Heat Transfer*, Vol. 122, No. 1, 2000, pp. 159–164.

[6]Ma, N., and Walker, J. S., "A Parametric Study of Segregation Effects During Vertical Bridgman Crystal Growth With an Axial Magnetic Field," *Journal of Crystal Growth*, Vol. 208, No. 1, 2000, pp. 757–771.

[7]Ma, N., and Walker, J. S., "Inertia and Thermal Convection During Crystal Growth With a Magnetic Field," *Journal of Thermophysics and Heat Transfer*, Vol. 15, No. 1, 2001, pp. 50–54.

[8]Tagawa, T., Authie, G., and Moreau, R., "Buoyant Flow in Long Vertical Enclosures in the Presence of a Strong Horizontal Magnetic Field. Part 1. Fully-Established Flow," *European Journal of Mechanics B—Fluids*, Vol. 21, No. 4, 2002, pp. 383–398.

[9]Davoust, L., Moreau, R., Cowley, M. D., Tanguy, P. A., and Bertrand, F., "Numerical and Analytical Modeling of the MHD Buoyancy-Driven Flow in a Bridgman Crystal Growth Configuration," *Journal of Crystal Growth*, Vol. 180, No. 3/4, 1997, pp. 422–432.

[10]Ma, N., and Walker, J. S., "Liquid-Metal Buoyant Convection in a Vertical Cylinder with a Strong Vertical Magnetic Field and with a Non-Axisymmetric Temperature," *Physics of Fluids*, Vol. 7, No. 8, 1995, pp. 2061–2071.

[11]Garandet, J. P., and Alboussière, T., "Bridgman Growth: Modelling and Experiments," *The Role of Magnetic Fields in Crystal Growth, Progress in Crystal Growth and Characterization of Materials*, edited by K. W. Benz, Vol. 38, No. 1/4, Elsevier Science, Oxford, U.K., 1999, pp. 73–132.

[12]Walker, J. S., "Models of Melt Motion, Heat Transfer, and Mass Transport During Crystal Growth with Strong Magnetic Fields," *The Role of Magnetic Fields in Crystal Growth, Progress in Crystal Growth and Characterization of Materials*, edited by K. W. Benz, Vol. 38, No. 1/4, Elsevier Science, Oxford, U.K., 1999, pp. 195–213.

[13]Hjellming, L. N., and Walker, J. S., "Melt Motion in a Czochralski Puller with an Axial Magnetic Field: Motion due to Buoyancy and Thermocapillarity," *Journal of Fluid Mechanics*, Vol. 182, 1987, pp. 335–368.

[14]Ramachandran, N., and Watring, D. A, "Convection Damping by an Axial Magnetic Field During the Growth of HgCdTe by Vertical Bridgman Method—Thermal Effects," AIAA Paper 97-0450, Jan. 1997.